ACS Catalysis

Research Article

pubs.acs.org/acscatalysis

Understanding Polyol Decomposition on Bimetallic Pt−Mo Catalysts—A DFT Study of Glycerol

Bin Liu,*[,‡] Mingxia Zhou,[‡] Maria K. Y. Chan,[§] and Jeffrey P. Greeley[†]

[‡]Department of Chemical Engineering, Kansas State University, Manhattan, Kansas 66506, United States

[§]Center for Nanoscale Materials, Argonne National Laboratory, Argonne, Illinois 60439, United States

[†]School of Chemical Engineering, Purdue University, West Lafayette, Indiana 47907, United States

Supporting Information

ABSTRACT: Catalytic dehydrogenation and C−C and C−O bond cleavage for glycerol decomposition on bimetallic Pt−Mo alloy model catalysts are studied using periodic density functional theory. The scaling relationship developed for monometallic systems for fast binding energy prediction has been tested and validated on both Pt-skin and Pt_3Mo-skin bimetallic surfaces. Using only the binding energies of atomic C and O for corresponding alloy surfaces, this simple relationship is shown to be an extremely efficient approach to speeding up the catalytic trend analysis for bimetallic alloy catalysts. Similar to Pt(111), it is found that the Pt-skin surface also favors dehydrogenation via C−H bond cleavage and faster C−C bond cleavage over C−O bond cleavage, but the overall activity decreases compared with pure Pt. On Pt_3Mo-skin surfaces, the overall reaction becomes much more exothermic, but Mo species significantly affect the selectivity by favoring the C−O bond cleavage. Thermodynamic analyses also predict that surface Mo species can be easily oxidized under typical reforming conditions, forming molybdate clusters and severely altering surface structures and potentially catalytic properties. Guided by experimental observations, this study also explores possible bifunctional characteristics for Pt−Mo bimetallic catalysts responsible for improved reforming activity and hydrogen production rates.

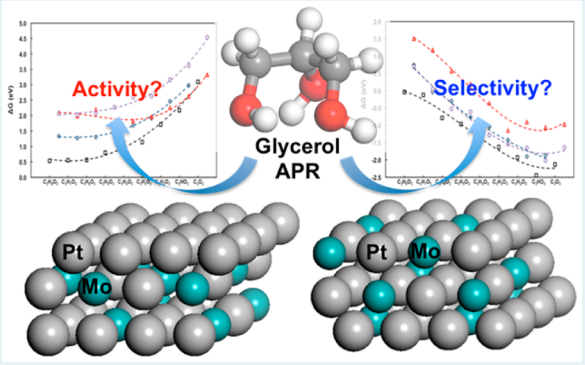

KEYWORDS: *density functional theory, genetic algorithm, glycerol decomposition, molybdenum oxide, Pt−Mo catalysts, scaling relationship*

1. INTRODUCTION

Hydrogen produced from aqueous phase reforming (APR) of oxygenated hydrocarbons, in particular polyols (e.g., ethylene glycol, glycerol, sorbitol, glucose) as shown in reactions 1 and 2, has been considered as one alternative route to obtain renewable fuels.[1−4] Even though platinum is considered an efficient catalyst for this purpose,[1] the use of pure Pt catalyst on a large scale is hindered by its high cost, low resistance to corrosion,[5,6] and low tolerance of CO poisoning.[7,8]

$$C_3H_8O_3(l) \rightarrow 3CO(g) + 4H_2(g) \quad \Delta H^0_{298K} = 350\ \text{kJ/mol} \tag{1}$$

$$CO(g) + H_2O(l) \rightarrow CO_2(g) + H_2(g) \quad \Delta H^0_{298K} = -41\text{kJ/mol} \tag{2}$$

All the above issues could pose major challenges for the implementation of catalytic hydrogen production from biomass-based materials. Given the intrinsic advantages of Pt for APR, the use of Pt−M alloys (M = Ni, Re, Co) as a strategy to tune the electronic properties of the host element (i.e., Pt) to overcome the above issues has been discussed in numerous recent studies.[2,9−13] In the search for new catalyst materials, the balance between catalytic hydrogen production activity and selectivity, such as reforming versus hydrogenolysis, dehydration, and methanation, is one of the main considerations. For instance, the TOF of glycerol APR on Pt−Re alloy increases by 10-fold, but the accompanying product distribution of alkane, alcohol, and organic acids can also be affected.[12,13]

Maximizing hydrogen production with special focus on developing bimetallic Pt catalysts is being actively studied.[11,14] Of particular relevance for the present study, the reforming rate has been significantly improved using Pt−Mo nanocatalysts.[15] Pt−Mo alloys have been studied as hydrocarbon hydrogenolysis catalysts[16,17] in which the hydrogenolysis activity is enhanced due to stronger binding of dehydrogenated hydrocarbon fragments in the presence of Mo.[17] The promotion of C−H bond cleavage ability with the addition of Mo was further demonstrated by Kariya et al., in which higher rates of hydrogen evolution via dehydrogenation of cyclohexanes were achieved, as compared with pure Pt.[18] In electrocatalysis, Pt−Mo alloys have

Received: December 29, 2014
Revised: July 13, 2015
Published: July 16, 2015

DOI: 10.1021/acscatal.5b01127
ACS Catal. 2015, 5, 4942−4950

been shown to help improve the anode tolerance to CO poisoning on a number of occasions,[19,20] and as described further below, they are have unusual properties for APR.

These phenomena can be attributed to the electronic and surface structural effects caused by Mo atoms. Nevertheless, these hypotheses have yet been confirmed with electronic structure calculations focusing on bimetallic Pt−Mo systems. In this study, we are going to apply a fast computational evaluation framework on the glycerol decomposition reaction network, which includes dehydrogenation, C−C bond cleavage, and C−O bond cleavage.

As demonstrated previously, analyses of trends in dehydrogenation, C−C, and C−O bond cleavage can be performed on monometallic surfaces without carrying out explicit density functional theory calculations on all reaction intermediates on monometallic catalysts.[21−23] Rather, the evaluation of reaction thermodynamics can be simplified by focusing on the relative binding energies of atomic C and O species, which are then correlated with the interactions of unsaturated atoms in the glycerol intermediates with metal surfaces. The Brønsted−Evans−Polanyi (BEP) relationship, in turn, provides reasonable estimates of the reaction kinetics.[24−26] Such an approach could also be useful in evaluating glycerol decomposition chemistry on bimetallic alloys in search of potentially promising candidates for more detailed analysis. To demonstrate this methodology, this study combines the above computational framework to evaluate the reaction thermodynamics and kinetics for glycerol decomposition on Pt−Mo alloys on two representative alloy surface configurations.

This work will also seek to elucidate the mechanism that leads to the increased reforming activity by identifying the active sites and possible catalyst configurations, with an emphasis on the real reforming conditions under which surface oxidation and restructuring may occur. The thermodynamic analyses on relevant structures of Pt-skin and alloy-skin surfaces in an oxidative environment will be used to understand the influence of the catalytic structures on reactivity properties.

2. COMPUTATIONAL METHODS

2.1. Density Functional Theory Calculations. The Vienna Ab-initio Simulation Package (VASP)[27,28] was used to perform periodic DFT calculations for total energies and structure optimizations on periodic Pt−Mo alloy slabs with the close-packed (111) facet. The generalized gradient approximation (GGA) PW91 was used to describe the electron exchange correlation functional.[29,30] The interaction between the valence electrons and ionic cores was described by the projector augmented wave (PAW) method,[31,32] in which the kinetic energy cutoff is 340 eV. The Methfessel−Paxton scheme was used for the electronic smearing, with a smearing parameter of 0.2 eV.[33] The total energies were then extrapolated to $k_BT = 0$ eV. The convergence criterion for the total energy self-consistent iterations was 1×10^{-6} eV. The geometry optimization stops when the total force on the system was less than 0.02 eV/Å. All calculations, including the dipole corrections, were performed along the direction perpendicular to the (111) surface.

The surface slabs were represented by 3-layer $p(4 \times 4)$ unit cells, corresponding to a minimum of 1/16 monolayer (ML) coverage. Only the top layer was allowed to relax, with the bottom two layers fixed at the optimized bulk value. The lattice constant, at 3.98 Å, was obtained by optimizing a 4-atom face-centered cubic unit cell for Pt_3Mo ($L1_2$) because we assume that surface segregation occurs only in the near surface region, whereas the bulk of the catalyst nanoparticle maintains the well-mixed condition. The slab and its successive images were separated by a vacuum spacing of 25 Å. The Brillouin zone is sampled with a $2 \times 2 \times 1$ k-point mesh based on the Monkhorst−Pack scheme.[34] Some energy barriers are calculated using the climbing-image nudged elastic band (CI-NEB)[35,36] method combined with the dimer method.[37] The transition states are confirmed to have only one imaginary (negative) vibrational mode.

2.2. Scaling Correlation for Thermodynamics Estimation. A fast empirical scaling relationship, as shown in eq 1, has been used to analyze glycerol decomposition by focusing on the thermodynamically stable and kinetically accessible intermediates on Pt−Mo bimetallic surfaces.[21−23]

$$\mathrm{BE_M} = \mathrm{BE_{Pt}} + (\mathrm{BE_{C,M}} - \mathrm{BE_{C,Pt}}) \sum_i \nu_{\mathrm{C}i} + (\mathrm{BE_{O,M}} - \mathrm{BE_{O,Pt}}) \sum_i \nu_{\mathrm{O},i} \quad (1)$$

$$\nu_i = \frac{n_{\max} - n_{\mathrm{bond}}}{n_{\max}} \quad (2)$$

$$\mathrm{BE_{C_xH_yO_z}}* = \sum_i p_{\mathrm{C}i}\nu_{\mathrm{C}i}[1 + p_{\mathrm{CO}i}(1 - n_{\mathrm{CO}i})] + \sum_i p_{\mathrm{O}i}\nu_{\mathrm{O}i} + \sum_i p_{\mathrm{CiO}i}\nu_{\mathrm{C}i}[1 + p_{\mathrm{CO}i}(1 - n_{\mathrm{CO}i})]\nu_{\mathrm{O}i} + \mathrm{BE_{C_xH_{2x+2}O_z}}* \quad (3)$$

where $\mathrm{BE_{Pt}}$ represents the binding energy of any glycerol intermediate for Pt(111). Equation 2 provides the definition for the valence of C/O atoms in the intermediate molecules. $\mathrm{BE_{C,Pt}}$ and $\mathrm{BE_{O,Pt}}$ are the binding energies of atomic C and O on Pt(111), which are −7.42 and −4.59 eV and listed in Table 1.

Table 1. Binding Energies (in eV) and Site Preferences (in parentheses) for H, C, O, OH, and CO on Pure Pt, Pt-skin, and Pt_3Mo-Skin Surfaces[a]

species	pure Pt	Pt-skin	Pt_3Mo-skin
H	−2.83 (top)	−2.53 (fcc II)	−2.69 (fcc II)
C	−7.42 (fcc)	−6.34 (hcp II)	−7.17 (fcc II)
O	−4.59 (fcc)	−3.93 (fcc II)	−6.72 (top I)
OH	−2.52 (tilted-top)	−2.48 (tilted-top II)	−4.15 (tilted-top I)
CO	−1.92 (fcc)	−1.37 (top I)	−1.94 (top I)

[a]Gas phase adsorbates are used as the reference for binding energies.

$\mathrm{BE_{C,M}}$ and $\mathrm{BE_{O,M}}$ represent the binding energies of C and O on Pt−Mo alloy surfaces, also listed in Table 1. In eq 1, $\mathrm{BE_{Pt}}$ were obtained from either explicit DFT calculations or a bond-order-based scaling relationship, described in eq 3.[21,22] $\mathrm{BE_{C_xH_{2x+2}O_z}}*$ is defined as the binding energy of intermediate $C_xH_yO_z$ in eq 3. $\mathrm{BE_{C_xH_{2x+2}O_z}}*$ is the binding energy of fully hydrogenated gas phase reference molecules corresponding to the dehydrogenating species on Pt(111). $n_{\mathrm{CO}i}$ is a conditional parameter such that $n_{\mathrm{CO}i} = 1$ if the C atom in the polyol molecule is bonded to an O atom, and $n_{\mathrm{CO}i} = 0$ otherwise. The actual fitting parameters in eq 3 are $p_{\mathrm{C}i}$, $p_{\mathrm{O}i}$, $p_{\mathrm{CO}i}$, and $p_{\mathrm{CiO}i}$, obtained from fitting to DFT calculations on a subset of glycerol dehydrogenation intermediates. The overall standard error based on such fitting is <0.2 eV.

DOI: 10.1021/acscatal.5b01127
ACS Catal. 2015, 5, 4942−4950

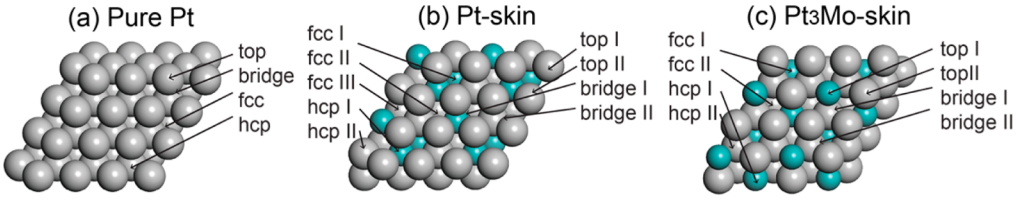

Figure 1. Schematic illustrations of Pt and Pt−Mo alloy $p(4 \times 4)$ unit cell: (a) pure Pt, (b) Pt-skin, and (c) Pt_3Mo-skin model. Pt and Mo atoms are represented with gray and turquoise spheres, respectively. High symmetry sites are labeled on each model.

The free energies are estimated by considering the entropy changes caused by the translational entropy (S_{trans}) lost and gained by adsorption of glycerol and desorption of hydrogen, according to eq 4.

$$S_{trans} = \frac{3}{2}R \ln\left(\frac{2\pi MkT}{h^2}\right) + R \ln \frac{kT}{P} + \frac{5}{2}R \quad (4)$$

where R is the gas constant, M is the molecular weight, k is the Boltzmann constant, h is the Planck's constant, T is the temperature (483 K), and P is the pressure (1 atm).

For our estimation, it is also assumed that the adsorbed hydrogen atoms are in the quasi-equilibrated state with the gas phase H_2 in the system. The entropy corrections of H_2 and glycerol in the gas phase are 0.64 and 0.88 eV for standard pressure and 483 K.

2.3. Brønsted−Evans−Polanyi Relationships. Instead of DFT calculations, the transition state energies of all the elementary steps for glycerol decomposition were estimated using the BEP relationship developed in our previous studies.[23] The BEP relationships are generally insensitive to surface elements and compositions; they are quite independent of the DFT functional used in calculations, as well.[26]

In this study, the slope and intercept for the BEP relationship describing dehydrogenation reactions are 1.05 (dimensionless) and 1.04 (in eV), with standard errors of 0.03 and 0.11 eV, respectively. For C−C and C−O bond cleavage, the corresponding values are 1.03 and 1.67 eV, with standard errors of 0.03 and 0.15 eV.

2.4. Genetic Algorithm (GA). A genetic algorithm developed for this study is used to explore the vast configurational space of O adsorption on the $p(4 \times 4)$ Pt-skin and Pt−Mo alloy surfaces over the range of surface coverage from 1/16 to 1 ML. This approach provides an efficient way to sample a large number of configurations and is not limited to high-symmetry sites (i.e., top, bridge, fcc, and hcp sites) on a given surface. The search procedure is initiated by generating 10−20 configurations for each coverage value. Local energy minimizations were performed using a conjugate gradient while constraining the adatoms to the surface to identify the five most stable configurations, which form the parents for the next generation. The next generation is then constructed on the basis of the geometric combinations of these parent structures, in addition to mutations formed by random perturbations of the structures. This search converges until no new low-energy configurations are identified. A GA run on the $p(2 \times 2)$ Pt−Mo unit cell has led to successful identification of a plausible global energy minimum configuration, which will be discussed in the following section.

3. RESULTS AND DISCUSSION

3.1. Pt−Mo Bimetallic Alloy Surfaces. Pure Pt, Pt-skin, and Pt_3Mo-skin configurations are schematically depicted in Figure 1. The Pt-skin model (Figure 1b), and Pt_3Mo-skin model (Figure 1c), both of which have the same Pt/Mo stoichiometric ratio of 3:1, are used to represent idealized models for the respective Pt-rich core−shell structure and the well-mixed alloy structure.

For the Pt-skin model, the composition can be represented as Pt−Pt_2Mo_2−Pt_3Mo (from the top layer to the bottom layer). To satisfy the stoichiometric ratio, Mo becomes more enriched in the in the second layer. The bottom layer (with Pt/Mo = 3:1) will represent the well-mixed bulk condition. For the Pt_3Mo-skin model, the bulk stoichiometric ratio, Pt_3Mo−Pt_3Mo−Pt_3Mo (also from top to bottom), is maintained throughout the study. The lattice constant for the unit cell is optimized on the basis of the fcc lattice of the $L1_2$ Pt_3Mo crystal structure.

Not all surface Pt atoms are catalytically equivalent because of the heterogeneity in the subsurface. In this work, type I Pt atoms are above the Pt−Mo−Mo 3-fold sites, and type II Pt atoms are above the Pt−Pt−Mo 3-fold sites (see Figure 1b). In the chosen Pt-skin model, types I and II Pt atoms form diagonal stripes. Accordingly, there are two types of bridge sites, two types of hcp sites, and three types of fcc sites on the surface (Figure 1b). For the Pt_3Mo-skin model, the high-symmetry adsorption sites are also indicated (Figure 1c). Several slabs with different Pt−Mo stoichiometry and atomic arrangements are also considered. The details of their composition and structure are shown in Figure S1 in the Supporting Information.

3.2. Adsorption of H, C, O, OH, and CO on Pt−Mo Surfaces. The binding energies of the central atoms, that is, C and O, are calculated according to $BE_X = E_{X*} - E_* - E_{X(g)}$ (X = C and O), where E_{X*} is the total energy of adsorbate on surface, E_* is the total energy of the clean surface, and $E_{X(g)}$ is the total energy of X in the gas phase. To derive the free energy diagrams, the adsorption of H, OH, and CO on Pt−Mo surfaces is also analyzed, and the binding energies and adsorption sites are also listed in Table 1. The most stable configuration and corresponding binding energies are shown in Figure 2 and Table 1.

On both Pt-skin and Pt_3Mo-skin surfaces, H adsorbs on the 3-fold fcc II site (Figure 2a, middle and right). Carbon adsorbs on the hcp II and fcc II sites of Pt-skin and Pt_3Mo-skin surfaces (Figure 2b, middle and right), respectively. Oxygen prefers the fcc II site of Pt-skin surface (Figure 2c, middle), but adsorbs on the top I (Mo) site of the Pt_3Mo-skin surface (Figure 2c, right). OH prefers the top Pt (top II) and Mo (top I) sites on Pt-skin and Pt_3Mo-skin surfaces (Figure 2d, middle and right), respectively. CO adsorbs on the Pt and Mo sites (both top I) of the respective Pt-skin and Pt_3Mo-skin surfaces (Figure 2e, middle and right).

On the Pt-skin surface, the binding energies of all the above species become weaker compared with the pure Pt surface (Table 1). In particular, the binding energy of C changes most significantly and decreases by more than 1 eV. It has been shown that typically, the adsorption energies of adsorbates (e.g., O) on the Pt overlayer tend to decrease when Pt is alloyed with a second

DOI: 10.1021/acscatal.5b01127
ACS Catal. 2015, 5, 4942−4950

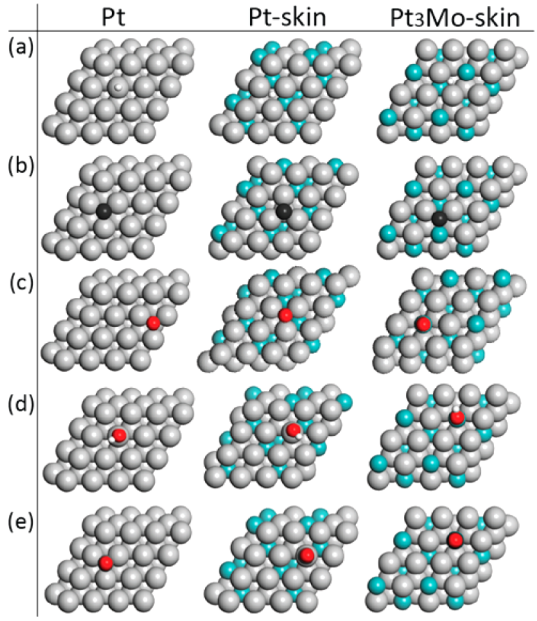

Figure 2. Optimized geometries on preferred adsorption sites of (a) H, (b) C, (c) O, (d) OH, and (e) CO adsorptions on pure Pt, Pt-skin, and Pt_3Mo-skin model surfaces. Spheres in gray, turquoise, black, white, and red represent Pt, Mo, C, H, and O atoms, respectively.

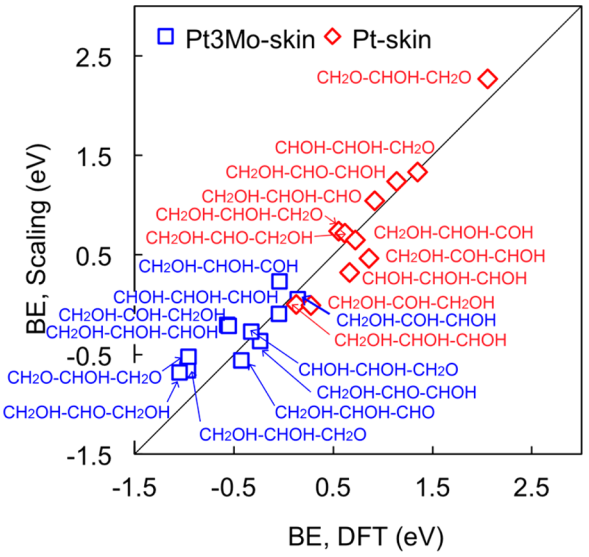

Figure 3. Comparison of the binding energies predicted using eq 1 for selected glycerol dehydrogenation intermediates (labeled in the Figure) on Pt-skin (red diamonds) and Pt_3Mo-skin (blue squares) with DFT calculations.

metal (e.g., Co, Fe, Ni).[38] In addition, the structural heterogeneity in bimetallic systems can influence adsorption site preference. For instance, the oxygen reduction by H on Pd−Ag alloys has been shown to be sensitive to such effects.[39] On the Pt_3Mo-skin model, the binding energies of atomic H and C are lower; CO binding energy is almost unaffected. The binding energies of O and OH become significantly stronger and increase by more than 2 and 1.5 eV, respectively.

3.3. Decomposition Intermediates on Bimetallic Surfaces. To validate eq 1 on bimetallic surfaces, explicit DFT calculations on 11 selected early stage dehydrogenation intermediates—either monodehydrogenated (four), or didehydrogenated intermediates (seven)—were performed on the Pt-skin and Pt_3Mo-skin surfaces. The binding energies directly calculated from DFT ($BE_{C_xH_yO_z*}$) are compared with BE_M predicted with eq 1 in Figure 3. BE_C and BE_O (in Table 1) on the two Pt−Mo alloy surfaces were used. The binding energy from DFT calculations ($BE_{C_xH_yO_z*}$) is defined as

$$BE_{C_xH_yO_z*} = E_{C_xH_yO_z*} - E_* - E_{C_xH_{2x+2}O_z(g)} + (2x - y + 2)E_{H_{2(g)}}/2 \quad (5)$$

where $E_{C_xH_{2x+2}O_z(g)}$ (where $x = 1-3$, and $y = 0-(2x+2)$) is the total energy of fully hydrogenated gas phase $C_xH_{2x+2}O_z$ ($z = 2-3$), and $E_{H_{2(g)}}$ is the total energy of gas phase H_2. The standard errors in Figure 3 are 0.16 and 0.25 eV for Pt-skin and Pt_3Mo-skin surfaces, respectively.

The optimized structures of the selected dehydrogenation intermediates are shown in Figure S2 in the Supporting Information. On Pt-skin surfaces, the adsorption preferences of unsaturated C and O species strongly resemble those on pure Pt; C binds to the sites that enable it to satisfy its valency of 4 (2 for O). The sublayer Mo atoms also play a subtle role in influencing the adsorbate orientations. For instance, the hydroxyl groups in a, b, d, e, f, g, i, and k in Figure S2 show preferences to interact with the Pt atoms (top II) aligned above the Mo rows in the sublayer.

On Pt_3Mo-skin surfaces, the site preference and orientation of adsorbates are controlled by the strong O−Mo interactions, where both the unsaturated O sites and the hydroxyl groups show an obvious preference for the top I (Mo) sites. The unsaturated C atoms, however, still prefer to bind to Pt species on the sites that will satisfy their valency.

On the basis of the behaviors of the considered intermediates, it is reasonable to believe that the predicted binding energies based on the linear scaling relationship will remain reliable, even given the simplicity of eq 2. In particular, there is strong evidence indicating that the valence rule for unsaturated C and O in the intermediates still applies on the Pt−Mo bimetallic alloys. It should be noted that the thermodynamics of glycerol decomposition estimated in this manner enables one to screen rapidly for catalytic trends.

3.4. Catalytic Trends of Glycerol Decomposition on Pt−Mo Alloys. On each monometallic surface (e.g., Pt, Pd, Rh, Ni, and Cu), it has been shown that BE_C and BE_O can be used to obtain qualitative insights on the thermochemistry for C−H bond versus O−H bond cleavage selectivity.[23,40] The results therein also indicate that this analysis can be extended to the kinetics of the glycerol decomposition network, as well, if coupled with transition state energies (using BEP relationships) of elementary steps. For glycerol decomposition, the catalytic activity and selectivity can be understood on the basis of the overall free energies, which are determined by the most stable reaction intermediates and the lowest energy barrier reaction steps (including all C−H, O−H, C−C, and C−O bond cleavage) formulated for each level of dehydrogenation. Below, we exploit the scaling relationship described above and adopt the same approach on the Pt-skin and Pt_3Mo-skin bimetallic models. Using clean surface and gas phase glycerol as the thermodynamic reference, the free energies of glycerol decomposition can then be summarized in the free energy diagrams (at 483 K and 1 atm) as shown in Figure 4.

All three diagrams include the free energy of adsorption of the most stable intermediates at each level of dehydrogenation (i.e.,

DOI: 10.1021/acscatal.5b01127
ACS Catal. 2015, 5, 4942−4950

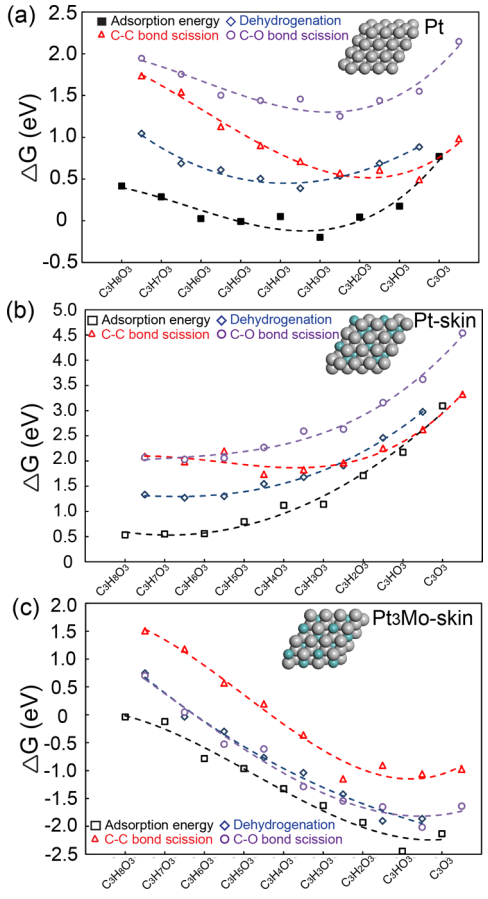

Figure 4. Free energy diagrams of glycerol decomposition on (a) pure Pt (adapted with permission from ref 22; Copyright Springer, 2012), (b) Pt-skin, and (c) Pt_3Mo-skin model surfaces (as labeled by the inset figures). The free energies of dehydrogenation intermediates (represented by black squares, solid for actual DFT calculations) are estimated at 483 K and 1 atm. The blue diamonds, red triangles, and purple circles represent the lowest transition state energies at each dehydrogenation level for dehydrogenation, C−C, and C−O bond cleavage. Dashed lines are used to highlight the trends.

$C_3H_xO_3$, $x = 0-8$), represented by black squares (solid symbols for actual DFT calculations). The lowest dehydrogenation transition state energies (either C−H or O−H bond cleavage) are represented by blue diamonds. The lowest transition state energies for C−C and C−O bond cleavage are represented by red triangles and purple circles, respectively. The dashed lines are added as guides to the eye. The diagram of glycerol decomposition on close-packed Pt(111) (adapted from ref 22) is included for the purpose of comparison and discussion. Figure 4a has shown that Pt is an active reforming catalyst for glycerol because the free energy favors the direction of dehydrogenation (exothermic). The kinetics for dehydrogenation (blue diamonds) and C−C bond cleavage (red triangles) are most competitive compared with the C−O bond cleavage (purple circles).[1,41] It should be noted that the combined dehydrogenation and C−C bond cleavage will favor the hydrogen selectivity.

Free energies of glycerol decomposition on Pt-skin surfaces are shown in Figure 4b. In the previous section, it was predicted using eq 1 that the binding energies of dehydrogenation intermediates will become weaker as a result of weaker C and O binding (Table 1). Consistent with this conclusion, in Figure 4b, the adsorption free energies increase monotonically as glycerol dehydrogenates. On the basis of the linear scaling relationship, eq 1, intermediates from the C−H bond cleavage are more stable than those from the O−H bond cleavage. By examining the transition state energies, where the average energy barrier can be estimated by the difference between the transition state energy and the adsorption free energy, it can be seen that the rates for dehydrogenation (mainly via C−H bond cleavage) are faster than both C−C and C−O bond cleavage at low levels of dehydrogenation (i.e., $x > 5$, as shown in Figure 4b). Nevertheless, the rate of dehydrogenation is likely to be lower (at 483 K and 1 atm) when compared to Pt because the overall dehydrogenation thermochemistry is much more endothermic. In addition, much more energy is needed for glycerol to achieve full dehydrogenation (right side of the free energy diagram). Once glycerol becomes substantially dehydrogenated (i.e., $x \leq 5$), the transition state energies of C−C bond cleavage become comparable to those of dehydrogenation. The decrease in the C−C bond cleavage energy barrier is enabled by decarbonylation, producing $C_2H_xO_2$ and CO. The decarbonylation becomes increasingly facile for highly dehydrogenated intermediates (i.e., $x \leq 3$), with energy barriers becoming even lower than for dehydrogenations. In contrast, across the reaction coordinates, the transition state energies of C−O bond cleavage remain relatively constant. In summary, in comparison with Figure 4a, the Pt-skin alloy surface shows higher endothermicity for glycerol decomposition and, therefore, much lower rates; however, the selectivity of the products results from dehydrogenation and C−C bond cleavage.

On a Pt_3Mo-skin surface, the dehydrogenation intermediates are produced from O−H bond cleavage, with energetics estimated according to eq 1. These intermediates will bind preferably on the Mo (top I) sites. As shown in Figure 4c, the overall thermochemistry becomes much more exothermic compared with pure Pt, mainly because of the strong O−Mo binding. Figure 4c shows that although dehydrogenation (via O−H) transition state energies are still low, the transition state energies of C−O bond cleavage also become competitive (almost coinciding with the dehydrogenation transition state energies). As a result of C−O bond cleavage, which prevents the formation of a carbonyl group, the C−C bond cleavage via decarbonylation is prohibited. As shown in Figure 4c, the transition state energies of C−C bond cleavage remain high throughout the reaction network. This observation indirectly supports the statement, discussed above for Pt-skins, that decarbonylation is the main route for C−C bond cleavage. In contrast to the Pt-skin surface, in the absence of surface site poisoning, the exothermicity, coupled with low energy barriers, on Pt_3Mo-skin would enable fast decomposition. However, the strong binding to surface Mo sites strongly suggests that the dissociated O or OH species will be difficult to remove and will most likely result in such poisoning. In addition, the C−O bond cleavage products eventually emerge as alkanes and alcohols, both of which can adversely affect the hydrogen selectivity.

In summary, catalytic trend analyses based on pure Pt, Pt-skin, and Pt_3Mo-skin surface models suggest very different catalytic activities, as well as product selectivities. Although detailed product distributions could, in theory, be determined with microkinetic modeling, a very large number of reaction intermediates and elementary steps make such an analysis impractical. Instead, we focus our analysis on the general energetic trends and on the elementary steps and intermediates that appear to govern the reactivity on the basis of these straightforward energetic analyses.

DOI: 10.1021/acscatal.5b01127
ACS Catal. 2015, 5, 4942−4950

3.5. Geometry and Energetics of O Adsorptions on Pt−Mo Alloys. For glycerol decomposition, the Pt-skin surface will have lower activity compared with pure Pt, and the Pt_3Mo-skin will significantly affect the selectivity for hydrogen production and may be susceptible to rapid oxygen poisoning. Neither model, however, can satisfactorily explain the observed enhanced turnover frequencies for both glycerol decomposition.[15] A likely explanation for these discrepancies lies with the possibility that Pt−Mo alloys could significantly reconstruct during exposure to air or under reaction conditions. In particular, the exothermicity and rapid C−O bond cleavage in the ambient condition could very well lead to significant surface restructuring, or even self-poisoning. To reconcile our modeling with experimental findings, we have analyzed such changes, and we predict that under real APR conditions, the Pt−Mo catalyst could, indeed, restructure and may possess regions with different catalytic functionalities. Oxidation and structural evolution of Mo species in the bimetallic system at reaction temperatures should be considered in this case.

Although both O and OH species bind strongly on the surface Mo sites and may exist under reaction conditions, any exposure of catalysts to air over time most likely will cause the formation of Mo oxides. Thus, as a first step toward understanding this problem and to preserve a tractable analysis, we focused only on the adsorption of O species. The O coverage values of 1/16, 1/8, 3/16, 1/4, 5/16, 3/8, 7/16, 1/2, 5/8, 3/4, and 1 ML, are studied using a combination of genetic algorithm and geometry optimizations. The most stable configuration corresponding to each coverage is shown in Figure 5.

The binding energy (in eV) per O atom for a certain coverage is defined as $BE = (E_{total} - E_* - N_{O*} \times E_{atom(g)})/N_{O*}$, where E_{total}, E_*, N_{O*}, and $E_{atom(g)}$ are the total energy of adsorption, clean surface, the number of O atoms, and total energy of the gas phase O atom, respectively. The differential binding energy (ΔBE, in eV), is defined as $\Delta BE = BE - BE_{1/16ML}$. Both BE and ΔBE are listed in Table 2.

As shown in Table 2, on the Pt-skin surface, the binding energy per O atom increases by 0.03 eV with each additional O atom up to 1/4 ML coverage. The small changes in this low O coverage regime indicate that the lateral interactions are negligible when the interatomic distances between O atoms are evenly distributed on the $p(4 \times 4)$ unit cell.[42] For O coverages between 1/4 ML and 1/2 ML, the binding energy starts to decrease (i.e., ΔBE increases). Up to 1/2 ML, O atoms still prefer the fcc II sites. At even higher O coverages (>1/2 ML), ΔBE is >0.28 eV. Oxygen atoms are found to occupy the fcc-I and fcc-III sites, as shown in Figure 5a. The lowest energy configurations indicate that surface Pt atoms can be dislocated from their lattice (as illustrated in the side view of 5/8 ML and 3/4 ML O coverage), an early sign of oxidation. At 1 ML, all O atoms adsorb onto the top Pt sites. Although no significant surface distortion is observed from DFT calculations, it is possible that, with finite temperature annealing (at APR conditions) or different unit cells, these configurations might exhibit segregation of Mo atoms (from subsurface) to the surface.

On Pt_3Mo-skin surfaces, O atoms show strong preference for the top I sites (Mo). At coverages below 1/4 ML, the binding energies per O atom remain constant (with ΔBE within 0.06 eV as shown in Table 2). Once all the top I (Mo) sites are occupied, surface Mo atoms continue to accept additional O atoms, resulting in higher oxidation states, such as $Mo(4+)O_2$ (e.g., at 5/16 ML in Figure 5B), $Mo(6+)O_3$ (e.g., at 3/8 ML in Figure 5b), and $Mo(8+)O_4$ (e.g., at 7/16 ML in Figure 5b). Mo can no longer be further oxidized once the MoO_4 structure is formed. A search of O adsorption configurations using our genetic algorithm shows that the tetrahedral MoO_4 structure is energetically stable. In Figure 5b, it can be seen that the Mo atoms are completely dislocated from their lattice, forming Mo−O−Pt bonds. Vacancy sites are produced underneath the dislocated Mo atoms. Most likely, these low-coordinated surface sites near the vacancy sites are expected to exhibit higher mobility

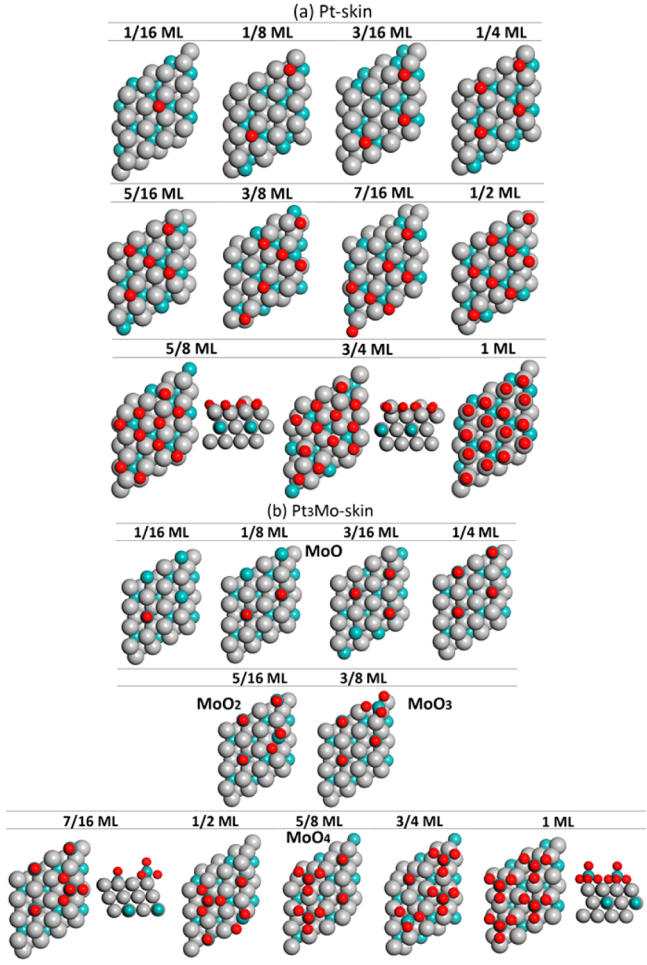

Figure 5. (a) Oxygen adsorption on Pt-skin surfaces; (b) Pt_3Mo-skin surfaces, where the oxidation states of Mo are also labeled. Gray, turquoise, and red spheres represent Pt, Mo, and O atoms.

Table 2. Binding Energies per O Atom and Differential Binding Energies of O Atom on Pt-Skin and Pt_3Mo-Skin Surfaces for Different Coverages

	Pt-skin		Pt_3Mo-skin	
coverage, ML	BE/O atom, eV	ΔBE, eV	BE/O atom, eV	ΔBE, eV
1/16	−3.93		−6.72	
1/8	−3.96	−0.03	−6.69	0.03
3/16	−3.96	−0.03	−6.67	0.05
1/4	−3.96	−0.03	−6.66	0.06
5/16	−3.89	−0.03	−6.38	0.34
3/8	−3.84	0.09	−6.19	0.53
7/16	−3.79	0.14	−6.05	0.67
1/2	−3.73	0.20	−5.93	0.79
5/8	−3.65	0.28	−5.75	0.97
3/4	−3.54	0.39	−5.63	1.09
1	−3.37	0.56	−5.48	1.24

DOI: 10.1021/acscatal.5b01127
ACS Catal. 2015, 5, 4942−4950

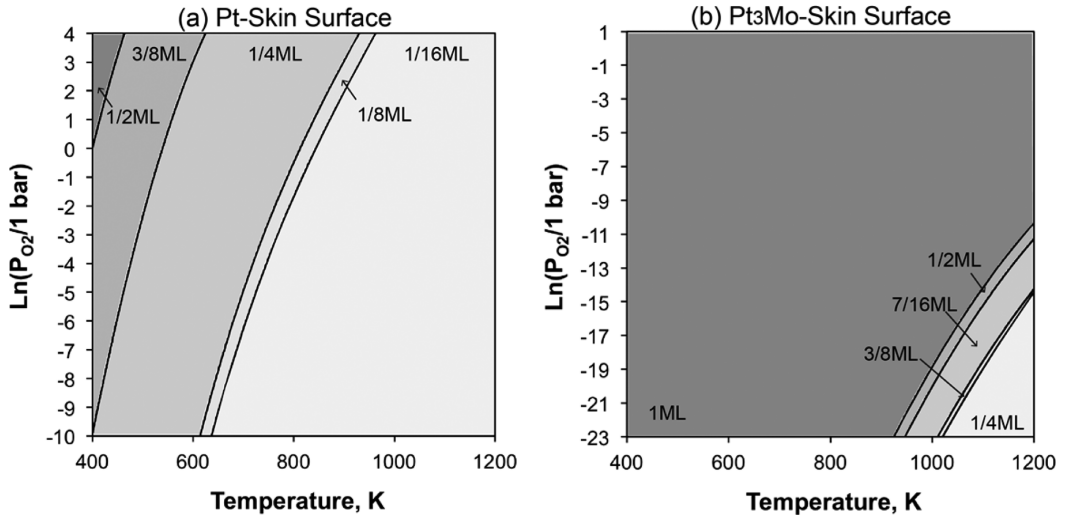

Figure 6. Phase diagrams of O adsorptions on (a) Pt-skin (4.5×10^{-5}, ~10^{2} bar, 400−1200 K); and (b) Pt_3Mo-skin (10^{-10}, ~ 3 bar, 400−1200 K) surfaces.

and will induce surface restructuring.[43−45] The considerations of oxidized surfaces after restructuring will be discussed in the following sections.

3.6. Free Energies of O Adsorptions on Pt−Mo Surfaces. A grand potential approach is used to study the thermodynamic surface stability for a range of pressures and temperatures,[46] as shown in Figure 6a,b. The details adopted in this study for estimating the free energies can be found in the Supporting Information.

For the entire temperature and pressure scanned, a maximum oxygen coverage of 1/2 ML has been attained on the Pt-skin surface in the low-temperature (<450 K) and high-pressure (>1 bar) regimes. The O atoms are arranged on the surface in an ordered configuration. Figure 6a also indicates that the thermodynamically equilibrated O coverage is lower than that on Pt(111) at the same temperature and pressure,[42] which is consistent with the fact that O binding becomes weaker on the Pt-skin alloy surface. With increasing temperature (over the entire pressure range scanned), the oxygen coverage transitioned from 1/2 ML to 3/8 ML to 1/4 ML to 1/8 ML to 1/16 ML. Under the APR conditions (i.e., 483 K, 1 bar), the O coverage is expected to be near the 3/8 ML region, according to this thermodynamic analysis.

On the Pt_3Mo-skin surface, as shown in Figure 6b, the free energy diagram is clearly dominated by the 1 ML coverage regime, corresponding to the configuration in which all surface Mo sites are in the form of highly oxidized molybdate (MoO_4). The 1 ML coverage is thermodynamically stable at pressures as low as 10^{-5} bar over the entire scanned temperature range. The free energy diagram shows that surface Mo species would be highly oxidized under the APR conditions. Even at extremely low oxygen pressure (e.g., UHV conditions), lower O coverage configurations are not possible unless the temperature is very high. Indeed, the lowest coverage attained in Figure 6b is 1/4 ML, where the temperature is above 1000 K (at 10^{-23} bar) and pressure is below 10^{-14} bar (at 1200 K). For the low to medium coverage configurations ($1/4\ \text{ML} \le \theta \le 1/2\ \text{ML}$), all the surface Mo atoms will still end up binding to at least one O atom.

3.7. Catalytic Functionalities of Oxidized Pt−Mo Alloys. The free energy diagrams (Figure 4) indicate that for glycerol decomposition, the activity can be too low on the Pt-skin surface or the hydrogen selectivity can be severely undermined on the Pt_3Mo-skin surface. Furthermore, O adsorption phase diagrams suggest that surface Mo species are likely to be oxidized. The thermodynamic predictions of alloy surface configurations in realistic APR conditions, especially on the Pt_3Mo-skin surface, indicate that additional functionality other than metal-catalyzed dehydrogenation, C−C, or C−O bond scission is required.

With metallic Pt sites continuing to enable effective dehydrogenation and C−C bond cleavage, the kinetics extracted from APR also proposed that the improved reforming turnover frequency with possible hydrogen production enhancement can be attributed to (1) improved tolerance toward CO poisoning due to weaker binding on the active Pt sites[47−51] and (2) promoted water−gas shift reaction by Mo oxides to consume CO and increase hydrogen production.[52,53]

The binding energies of CO listed in Table 1 already provide evidence that the poisoning of CO due to its strong binding at Pt sites can be mitigated on the alloy surface. In addition, CO can also be removed via water−gas shift reaction (WGSR). Detailed WGSR mechanisms on Pt were studied using DFT calculations,[54,55] which conclude that the carboxyl pathway is the main reaction route (see black paths in Figure 7). In this work, water

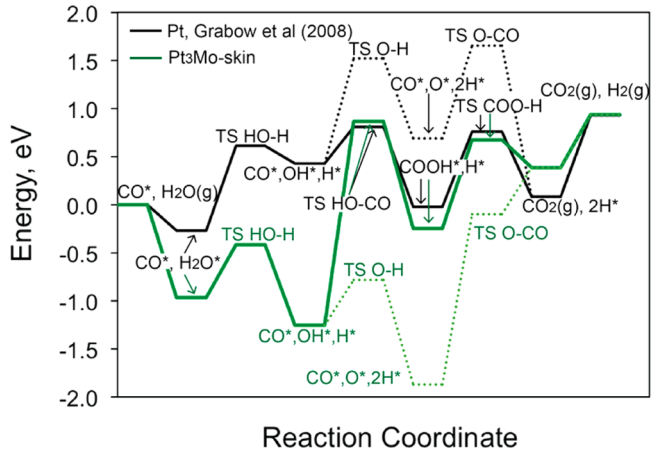

Figure 7. Potential energy surfaces of water dissociation and WGSR carboxyl (solid) and redox (dash) pathways on Pt (black) and Pt_3Mo-skin (green) (111) surfaces.

DOI: 10.1021/acscatal.5b01127
ACS Catal. 2015, 5, 4942−4950

dissociation and the carboxyl and redox pathways are studied on the Pt_3Mo-skin surfaces to understand the performance of unoxidized surface Mo species in WGSR. In Figure 7, adsorbed CO (treated as a reforming product) and gas phase H_2O are used as the calculation reference. The molecular structures involved in water dissociation, the carboxyl, and redox pathways are shown in Figure S3 in the Supporting Information.

Water activation on Pt(111) can influence the rate of WGSR on Pt surfaces. The adsorption energy of water is −0.96 eV (on the top I site), much stronger than that of −0.27 eV on Pt(111). Successive water dissociation steps (green solid and dashed paths) are more exothermic, at −0.29 eV and −0.62 eV, compared with that on Pt(111) at 0.7 and 0.26 eV. The dissociation energy barriers are also much lower, at 0.54 and 0.47 eV, than on the corresponding Pt(111) surface (0.88 and 1.09 eV). It can be concluded that the water dissociation becomes much more facile, and the production of O and OH species for subsequent WGSR is facilitated.

Despite more abundant O and OH species on the Pt_3Mo-skin surface, however, the formation of both COOH and CO_2 are slowed down due to increased energy barriers, at 2.12 and 1.77 eV, and also due to the strong endothermic character (1.0 and 2.25 eV, respectively) compared with the Pt(111). This can be explained by the fact that C−O bond formations in both carboxyl and redox pathways require the cleavage of strong Mo−O bonds. For this reason, the metallic Mo site alone seems unlikely to be the main active sites in promoting WGSR in APR.

Given that Mo species are oxophilic and Mo oxides are readily available on catalyst surfaces, the formation of COOH and CO_2 is studied with a MoO_4 cluster supported on Pt−Mo alloy surfaces, as shown in Figure S3. With MoO_4, the energetics for COOH and CO_2 formation become less endothermic, at 0.46 and 0.96 eV, respectively, also with significantly lower energy barriers of 1.27 and 0.91 eV than on the Pt_3Mo-skin surface. These calculations further indicate that, instead of metallic Mo, Mo oxide on the bimetallic catalyst surface may actually play the main role in oxidizing and removing adsorbed CO (which may be regenerated partly by water dissociation after CO reduction).

It is important to note that a fully detailed comparison with experimentally observed Pt−Mo nanocatalyst structures is challenging, largely because of the fact that real catalyst particles have complex phases. Nevertheless, existing in situ characterization techniques show that reduced Pt−Mo alloys have a Pt-rich core (~25% Pt surface) and a Mo-rich (oxide) surface,[56] consistent with the O adsorption phase diagram predicted on the Pt_3Mo-skin surface. The catalytic properties from glycerol APR experiments indicate that at low glycerol conversion, the TOF has been improved compared with pure Pt catalysts. The selectivity of hydrogen production and C−O bond cleavage can be affected at higher conversion, where methane production, as a result of C−O bond cleavage, is increased.[56,57] In addition, WGSR can be promoted by a Mo-rich surface Pt−Mo alloy catalyst, in which a certain amount of Mo species can act as the promoter for the reaction.[52] These observations are broadly consistent with our surface models that point to the importance of bifunctionality in glycerol APR reactions on Pt−Mo alloy surfaces.

4. CONCLUSIONS

Periodic DFT calculations, combined with fast energetic and kinetic analyses, were used to investigate glycerol decomposition on bimetallic Pt−Mo alloy surfaces. The scaling relationship developed for monometallic surfaces, such as Pt, Pd, Rh, and Ni, is extended and applied to Pt-skin alloy surfaces. The scaling relationship is little affected by the presence of a much stronger binding site (Mo) to oxygen or oxygenated species, such as OH or unsaturated O sites, in the intermediates. Hence, the scaling relationship, which is based on the approximate bond-order conservation concept, can serve as an accelerated approach for heterogeneous catalytic trend analysis for Pt-based bimetallic catalysts.

For Pt skins on Pt−Mo alloys, dehydrogenation remains kinetically competitive, and C−C bond cleavage selectivity stays higher than that for C−O bond cleavage. However, because of overall weaker C and O binding, the dehydrogenation, C−C, and C−O bond cleavage in glycerol decomposition become more endothermic, thus reducing activity. The presence of surface Mo species, on the other hand, can significantly affect reforming selectivity. Because of much stronger binding of O-containing species on the surface Mo sites, C−O bond cleavage becomes much more favored energetically.

In addition, a surface containing Mo sites can be easily oxidized. The formation of MoO_x ($x = 2-4$) clusters can lead to substantial surface restructuring, resulting in segregation of the molybdenum oxide phase from the remaining metallic Pt phase. The Mo oxide may change the mechanism of the water−gas shift reaction associated with APR, whereas Pt will be involved in the initial glycerol dehydrogenation and C−C bond cleavage. In summary, this study on glycerol decomposition suggests a potentially significant bifunctionality possessed by Pt−Mo bimetallic catalysts.

■ ASSOCIATED CONTENT

Supporting Information

The Supporting Information is available free of charge on the ACS Publications website at DOI: 10.1021/acscatal.5b01127.

Additional figures, table, and scheme and computational details (PDF)

■ AUTHOR INFORMATION

Corresponding Author

*E-mail: binliu@ksu.edu.

Notes

The authors declare no competing financial interest.

■ ACKNOWLEDGMENTS

This work is supported in part by a Start-up fund provided by Kansas State University, the National Science Foundation under Award No. EPS-0903806, and matching support from the State of Kansas through the Kansas Board of Regents. Use of the Center for Nanoscale Materials, an Office of Science user facility, was supported by the U.S. Department of Energy, Office of Science, Office of Basic Energy Sciences under Contract No. DE-AC02-06CH11357. We gratefully acknowledge the computing resources provided on Fusion, a high-performance computing cluster operated by the Laboratory Computing Resource Center at Argonne National Laboratory. We also acknowledge computational resources provided by Beocat Research Cluster at Kansas State University, which is funded in part by NSF Grants CNS-1006860 and the National Energy Research Scientific Computing Center (NERSC) under Contract No. DE-AC02-05CH11231.

DOI: 10.1021/acscatal.5b01127
ACS Catal. 2015, 5, 4942−4950

REFERENCES

(1) Cortright, R. D.; Davda, R. R.; Dumesic, J. A. *Nature* **2002**, *418*, 964−967.
(2) Huber, G. W.; Shabaker, J. W.; Dumesic, J. A. *Science* **2003**, *300*, 2075−2077.
(3) Tanksale, A.; Beltramini, J. N.; Lu, G. M. *Renewable Sustainable Energy Rev.* **2010**, *14*, 166−182.
(4) Wei, Z.; Sun, J.; Li, Y.; Datye, A. K.; Wang, Y. *Chem. Soc. Rev.* **2012**, *41*, 7994−8008.
(5) Roen, L. M.; Paik, C. H.; Jarvi, T. D. *Electrochem. Solid-State Lett.* **2004**, *7*, A19−A22.
(6) Ferreira, P. J.; la O', G. J.; Shao-Horn, Y.; Morgan, D.; Makharia, R.; Kocha, S.; Gasteiger, H. A. *J. Electrochem. Soc.* **2005**, *152*, A2256−A2271.
(7) McNicol, B. D.; Rand, D. A. J.; Williams, K. R. *J. Power Sources* **1999**, *83*, 15−31.
(8) Soares, R. R.; Simonetti, D. A.; Dumesic, J. A. *Angew. Chem., Int. Ed.* **2006**, *45*, 3982−3985.
(9) Wang, X.; Li, N.; Pfefferle, L. D.; Haller, G. L. *Catal. Today* **2009**, *146*, 160−165.
(10) Tanksale, A.; Beltramini, J. N.; Dumesic, J. A.; Lu, G. Q. *J. Catal.* **2008**, *258*, 366−377.
(11) Skoplyak, O.; Menning, C. A.; Barteau, M. A.; Chen, J. G. G. *Top. Catal.* **2008**, *51*, 49−59.
(12) King, D. L.; Zhang, L.; Xia, G.; Karim, A. M.; Heldebrant, D. J.; Wang, X.; Peterson, T.; Wang, Y. *Appl. Catal., B* **2010**, *99*, 206−213.
(13) Zhang, L.; Karim, A. M.; Engelhard, M. H.; Wei, Z.; King, D. L.; Wang, Y. *J. Catal.* **2012**, *287*, 37−43.
(14) Skoplyak, O.; Barteau, M. A.; Chen, J. G. *ChemSusChem* **2008**, *1*, 524−526.
(15) Dietrich, P. J.; Lobo-Lapidus, R. J.; Wu, T. P.; Sumer, A.; Akatay, M. C.; Fingland, B. R.; Guo, N.; Dumesic, J. A.; Marshall, C. L.; Stach, E.; Jellinek, J.; Delgass, W. N.; Ribeiro, F. H.; Miller, J. T. *Top. Catal.* **2012**, *55*, 53−69.
(16) Yermakov, Y. I.; Kuznetsov, B. N.; Ryndin, Y. A. *J. Catal.* **1976**, *42*, 73−78.
(17) Tri, T. M.; Massardier, J.; Gallezot, P.; Imelik, B. *J. Catal.* **1984**, *85*, 244−252.
(18) Kariya, N.; Fukuoka, A.; Ichikawa, M. *Appl. Catal., A* **2002**, *233*, 91−102.
(19) Massong, H.; Wang, H. S.; Samjeske, G.; Baltruschat, H. *Electrochim. Acta* **2001**, *46*, 701−707.
(20) Papageorgopoulos, D. C.; Keijzer, M.; de Bruijn, F. A. *Electrochim. Acta* **2002**, *48*, 197−204.
(21) Liu, B.; Greeley, J. *J. Phys. Chem. C* **2011**, *115*, 19702−19709.
(22) Liu, B.; Greeley, J. *Top. Catal.* **2012**, *55*, 280−289.
(23) Liu, B.; Greeley, J. *Phys. Chem. Chem. Phys.* **2013**, *15*, 6475−6485.
(24) Wang, S.; Petzold, V.; Tripkovic, V.; Kleis, J.; Howalt, J. G.; Skulason, E.; Fernandez, E. M.; Hvolbaek, B.; Jones, G.; Toftelund, A.; Falsig, H.; Bjorketun, M.; Studt, F.; Abild-Pedersen, F.; Rossmeisl, J.; Norskov, J. K.; Bligaard, T. *Phys. Chem. Chem. Phys.* **2011**, *13*, 20760−20765.
(25) Wang, S.; Temel, B.; Shen, J.; Jones, G.; Grabow, L. C.; Studt, F.; Bligaard, T.; Abild-Pedersen, F.; Christensen, C. H.; Norskov, J. K. *Catal. Lett.* **2011**, *141*, 370−373.
(26) Liu, B.; Cheng, L.; Curtiss, L.; Greeley, J. *Surf. Sci.* **2014**, *622*, 51−59.
(27) Kresse, G.; Hafner, J. *Phys. Rev. B: Condens. Matter Mater. Phys.* **1993**, *47*, 558−561.
(28) Kresse, G.; Furthmuller, J. *Phys. Rev. B: Condens. Matter Mater. Phys.* **1996**, *54*, 11169−11186.
(29) Perdew, J. P.; Ziesche, P., Eschrig, H., Eds.; *Electronic Structure of Solids '91*, Akademie: Berlin, 1992; p 11.
(30) Perdew, J. P.; Chevary, J. A.; Vosko, S. H.; Jackson, K. A.; Pederson, M. R.; Singh, D. J.; Fiolhais, C. *Phys. Rev. B: Condens. Matter Mater. Phys.* **1992**, *46*, 6671−6687.
(31) Blochl, P. E. *Phys. Rev. B: Condens. Matter Mater. Phys.* **1994**, *50*, 17953−17979.
(32) Kresse, G.; Joubert, D. *Phys. Rev. B: Condens. Matter Mater. Phys.* **1999**, *59*, 1758−1775.
(33) Methfessel, M.; Paxton, A. T. *Phys. Rev. B: Condens. Matter Mater. Phys.* **1989**, *40*, 3616−3621.
(34) Monkhorst, H. J.; Pack, J. D. *Phys. Rev. B* **1976**, *13*, 5188−5192.
(35) Henkelman, G.; Johannesson, G.; Jonsson, H.; *Methods for Finding Saddle Points and Minimum Energy Paths*, Kluwer Academic: New York, 2000; p 269.
(36) Henkelman, G.; Jonsson, H. *J. Chem. Phys.* **2000**, *113*, 9978−9985.
(37) Henkelman, G.; Jonsson, H. *J. Chem. Phys.* **1999**, *111*, 7010−7022.
(38) Stamenkovic, V.; Mun, B. S.; Mayrhofer, K. J. J.; Ross, P. N.; Markovic, N. M.; Rossmeisl, J.; Greeley, J.; Norskov, J. K. *Angew. Chem., Int. Ed.* **2006**, *45*, 2897−2901.
(39) Farberow, C. A.; Godinez-Garcia, A.; Peng, G. W.; Perez-Robles, J. F.; Solorza-Feria, O.; Mavrikakis, M. *ACS Catal.* **2013**, *3*, 1622−1632.
(40) Mehmood, F.; Rankin, R. B.; Greeley, J.; Curtiss, L. A. *Phys. Chem. Chem. Phys.* **2012**, *14*, 8644−8652.
(41) Davda, R. R.; Alcala, R.; Shabaker, J.; Huber, G.; Cortright, R. D.; Mavrikakis, M.; Dumesic, J. A. In *Science and Technology in Catalysis 2002*; Anpo, M., Onaka, M., Yamashita, H., Eds.; Kodansha Ltd: Tokyo, 2003; Vol. *145*, p 79−84.
(42) Getman, R. B.; Xu, Y.; Schneider, W. F. *J. Phys. Chem. C* **2008**, *112*, 9559−9572.
(43) Stranick, S. J.; Parikh, A. N.; Allara, D. L.; Weiss, P. S. *J. Phys. Chem.* **1994**, *98*, 11136−11142.
(44) Greeley, J.; Nørskov, J. K. *Electrochim. Acta* **2007**, *52*, 5829−5836.
(45) Greeley, J. *Electrochim. Acta* **2010**, *55*, 5545−5550.
(46) Greeley, J.; Mavrikakis, M. *Surf. Sci.* **2003**, *540*, 215−229.
(47) Ioroi, T.; Akita, T.; Yamazaki, S.; Siroma, Z.; Fujiwara, N.; Yasuda, K. *Electrochim. Acta* **2006**, *52*, 491−498.
(48) Ioroi, T.; Fujiwara, N.; Siroma, Z.; Yasuda, K.; Miyazaki, Y. *Electrochem. Commun.* **2002**, *4*, 442−446.
(49) Ioroi, T.; Yamazaki, S. I.; Siroma, Z.; Fujiwara, N.; Yasuda, K. *Electrochemistry* **2007**, *75*, 159−162.
(50) Kwiatkowski, K. C.; Milne, S. B.; Mukerjee, S.; Lukehart, C. M. *J. Cluster Sci.* **2005**, *16*, 251−272.
(51) Mukerjee, S.; Urian, R. C.; Lee, S. J.; Ticianelli, E. A.; McBreen, J. *J. Electrochem. Soc.* **2004**, *151*, A1094−A1103.
(52) Williams, W. D.; Bollmann, L.; Miller, J. T.; Delgass, W. N.; Ribeiro, F. H. *Appl. Catal., B* **2012**, *125*, 206−214.
(53) Dietrich, P. J.; Wu, T. P.; Sumer, A.; Dumesic, J. A.; Jellinek, J.; Delgass, W. N.; Ribeiro, F. H.; Miller, J. T. *Top. Catal.* **2013**, *56*, 1814−1828.
(54) Grabow, L. C.; Gokhale, A. A.; Evans, S. T.; Dumesic, J. A.; Mavrikakis, M. *J. Phys. Chem. C* **2008**, *112*, 4608−4617.
(55) Clay, J. P.; Greeley, J. P.; Ribeiro, F. H.; Delgass, W. N.; Schneider, W. F. *J. Catal.* **2014**, *320*, 106−117.
(56) Dietrich, P. J.; Lobo-Lapidus, R. J.; Wu, T.; Sumer, A.; Akatay, M. C.; Fingland, B. R.; Guo, N.; Dumesic, J. A.; Marshall, C. L.; Stach, E.; Jellinek, J.; Delgass, W. N.; Ribeiro, F. H.; Miller, J. T. *Top. Catal.* **2012**, *55*, 53−69.
(57) Dietrich, P. J.; Wu, T.; Sumer, A.; Dumesic, J. A.; Jellinek, J.; Delgass, W. N.; Ribeiro, F. H.; Miller, J. T. *Top. Catal.* **2013**, *56*, 1814−1828.

DOI: 10.1021/acscatal.5b01127
ACS Catal. 2015, 5, 4942−4950